Quantitative Local State of Charge Mapping by *Operando* Electrochemical Fluorescence Microscopy in Porous Electrodes

Anton M. Graf[a,†], Thomas Cochard[a,†], Kiana Amini[a,b], Michael S. Emanuel[a], Shmuel M. Rubinstein[*,c] and Michael J. Aziz[*,a]

a. *Harvard John A. Paulson School of Engineering and Applied Sciences, 29 Oxford St., Cambridge, MA02138, USA.*

b. *Present address: Department of Materials Engineering, University of British Columbia, Vancouver, BC Canada V6T 1Z4*

c. *Racah Institute of Physics, The Hebrew University of Jerusalem, Jerusalem, Israel.*

† These authors contributed equally to this work.

Electronic Supporting Information (ESI)

33   **ESI 1: Electrochemical setup and electrolyte preparation**

34

35   *Fabrication of the electrochemical cell:* The electrochemical cell was constructed by assembling

36   two acrylic plates, which sandwiched two Polydimethylsiloxane (PDMS) half-cells separated by

37   a Nafion 212 membrane, as illustrated in Figure S1(A). The PDMS components were fabricated

38   through 3D printing and molding. Initially, a mold design was created, and 3D printed using

39   Stereolithography (Form 3, Formlabs). Subsequently, PDMS was poured into each mold and

40   subjected to vacuum treatment to eliminate any air bubbles that could compromise transparency

41   and proper sealing of the components. The PDMS parts were then cured overnight at 65°C. Figure

42   S1(B) showcases the transparency achieved with the PDMS 3D printed mold. To assemble the

43   PDMS half-cells, electrodes, and membrane, transparent acrylic endplates and screws were used

44   to compress the components.

45
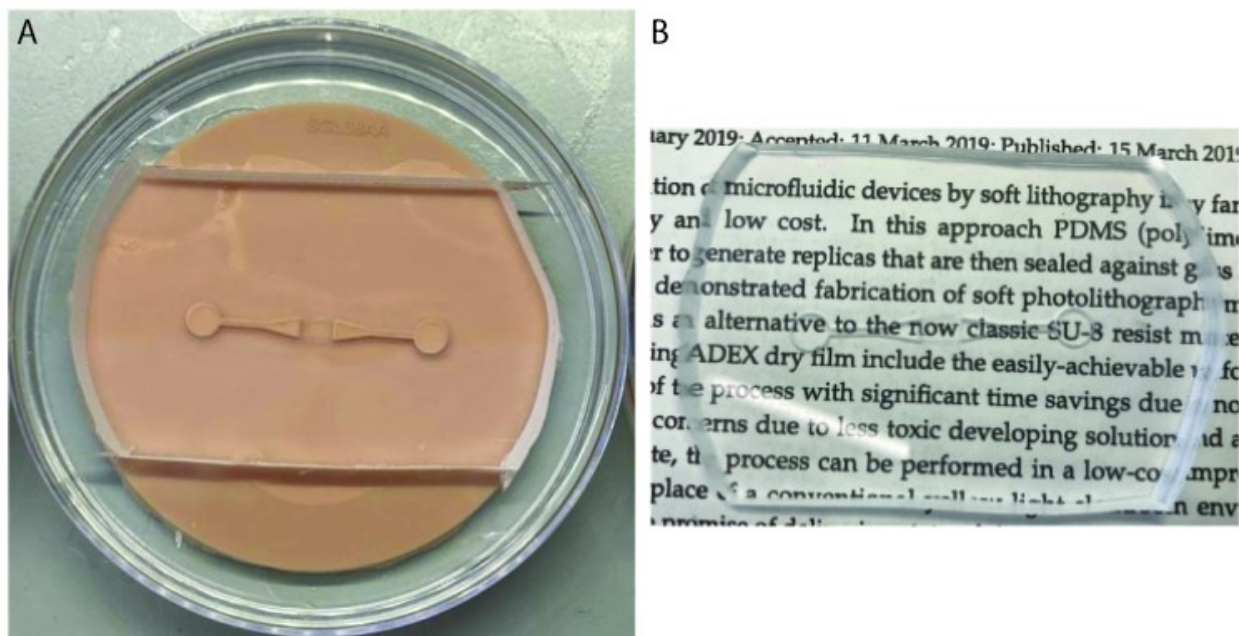
46

47   **Figure S1:** PDMS molding process. (A**)** 3D printed mold for the AQDS side with the flow channel feature in the center (orange

48   disk) in a petri-dish where the PDMS is poured. (B**)** AQDS side half-cell removed from the mold after curing. The transparency

49   of the pieces obtained is showcased by the text which is clearly readable.

50

51   *Electrolyte:* For the electrolyte concentration series, a 40 mM stock solution was prepared by

52   dissolving 2,7 anthraquinone disulfonate (AQDS) salt in 1M sulfuric acid. AQDS with a purity of

53   98% was procured from BocSciences. Electrolyte solutions of 40, 30, 20, and 10 mM were

54 obtained by diluting the stock solution with 1M sulfuric acid. To eliminate oxygen from the

55 electrolyte, each solution was purged with nitrogen (N2, ultra-high purity, Airgas) for 30 minutes

56 prior to each experiment. The electrochemical cell itself was also purged with nitrogen for 30

57 minutes, bringing the system to operating pressures to ensure the absence of leaks and remove any

58 remaining oxygen. In all experiments detailed in this report, the electrolyte was continuously

59 pumped through the cell at a constant flow rate of 2 mm/sec using a Harvard syringe pump. Further

60 information can be found in the main text.

61

62 *Electrochemical experiments:*

63 AvCarb MGL 190 carbon paper of nominal thickness 190 μm was used as the working electrode.

64 The electrode was baked for 24 h at 400 °C prior to the experiment. On the counter electrode side,

65 a 0.5 mg/cm² 60% Platinum on Vulcan - Carbon Paper Electrode from FuelCellStore was used to

66 oxidize hydrogen gas. Nafion 212, used as membrane, was soaked in 1 M sulfuric acid prior to the

67 experiments.

68   For the electrochemical experiments, a portable Gamry Instruments Reference 3000

69 potentiostat/galvanostat/ZRA was employed. The electrochemical reaction was induced using a

70 multi-step chronoamperometry protocol. Initially, the open circuit potential (OCV) was

71 determined for the two-electrode configuration of the hybrid cell. Subsequently, incremental

72 potential steps were applied and maintained at a constant value for 60 seconds each. In between

73 each potential step, the cell was purged at OCV conditions for 30 seconds. A sampling rate of 0.5

74 seconds was employed.

75

76 **ESI 2: *In situ* confocal microscopy**

77

78 Fluorescence microscopy was conducted using a spinning disk microscope while the

79 electrochemical flow cell was in operation. The setup consisted of a Leica MDi8 microscope body

80 and an Andor CSU-W spinning disk system. A Leica 10x/0.3NA HC PL FLUOTAR lens was

81 employed for imaging.

82 For all experiments presented in this study, the following parameters were utilized: a pinhole size

83 of 50 μm, an exposure time of 2 seconds, and an acquisition time of 2.5 seconds per frame.

84

85 Excitation light at a wavelength of 405 nm was provided by a laser, and emission light was filtered
86 through a green bandpass filter (approximately 475-525 nm). The laser intensity was set to 50%
87 of its maximum capacity. No gain or offset was applied. The laser was consistently on with the
88 exposure time mentioned above. The intensity and exposure time are crucial for controlling image
89 brightness. These parameters were adjusted to optimize the number of discrete intensity values
90 across the grayscale (each image was captured at 16-bit depth, corresponding to 65,536 gray
91 levels), ensuring optimal brightness.

92

93 **ESI 3: *Ex-situ* photophysical characterization**

94

95 The photophysical experiments involving emission and absorption scans were conducted using a
96 BioTek Synergy HT plate reader equipped with a 405 nm excitation source and an emission scan
97 capability. In each well of a GREINER MICROPLATE (96 WELL, PS, F-BOTTOM, µCLEAR®,
98 BLACK, MED. BINDING), 200 µL of each sample was loaded.

99 We prepared the 40 mM AQDS solutions following the procedure outlined in ESI 1. These
100 solutions were then transferred to a glovebox and subjected to charging versus V3+/V4+ under a
101 nitrogen (N2) atmosphere inside a bench-scale flow battery. The 40 mM solution was charged to
102 SOCs of 0%, 30%, 40%, 60%, 70%, 80%, and 90% and results are shown in the main text. For the
103 ex-situ tests, flow battery experiments utilized cell components sourced from Fuel Cell
104 Technologies Inc. (Albuquerque, NM). Each half-cell of the battery was equipped with
105 interdigitated flow fields made from pyro-sealed POCO graphite flow plates, with 3 layers of
106 carbon paper (SGL 39AA) per side, baked at 400 °C overnight. During cell assembly, the applied
107 torque was 60 lb-in (6.78 N·m) across eight 3/8"–24 bolts, resulting in a load of approximately
108 800 lbs per bolt. The geometric area of each electrode was 5 cm². A Nafion 212 cation exchange
109 membrane and a 10 mil Viton gasket separated the two half-cells. The cells were operated inside
110 a nitrogen-filled glovebox. To ensure accuracy, each solution underwent two battery cycles,
111 resulting in a consistent charge efficiency of 98% for all solutions, thereby minimizing systematic
112 errors. To prevent reoxidation due to the diffusion of atmospheric oxygen into the electrolytes, the
113 electrolyte solutions were transferred to a well plate inside the glovebox and sealed with a lid.

114

115 **ESI 4: 1:1 (AQDS:H$_2$AQDS) binding dimer model**

116

117 The quinhydrone concentration at each SOC value can be calculated from a system of equations.

118 Using the equilibrium constant of dimer formation of $K_{dim} = 80\ M^{-1}$ from the literature(1) and

119 the total concentration of the reactants participating in the electrochemical reaction, which is equal

120 to the initial concentration of AQDS in each experiment, a parametric curve for each species

121 concentration as a function of SOC can be computed. The system of equations is shown below:

$$K_{dim} = 80\ M^{-1} = \frac{[QH]}{[AQDS][H_2AQDS]} \tag{S4.1}$$

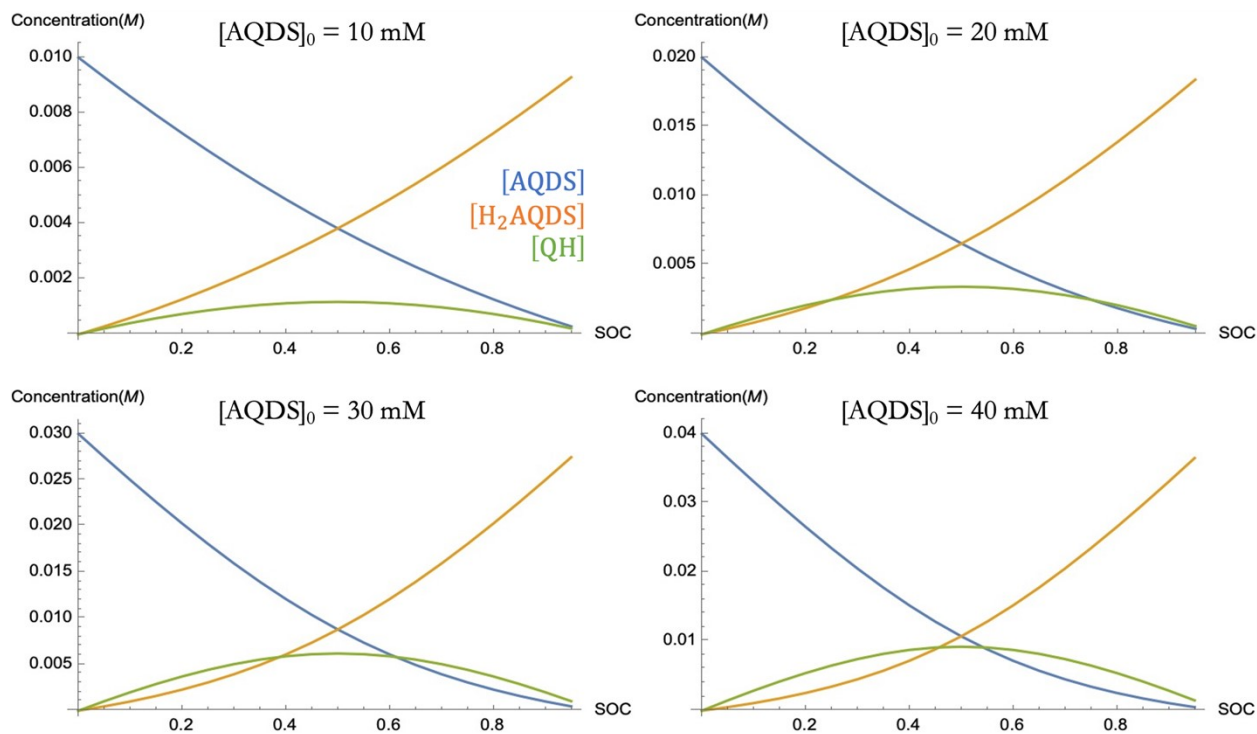122

$$[AQDS]_0 = [AQDS] + [H_2AQDS] + 2[QH] \tag{S4.2}$$

123

$$SOC = \frac{[H_2AQDS] + [QH]}{[AQDS] + [H_2AQDS] + 2[QH]} \tag{S4.3}$$

124
125 The system of equations is solved for different $[AQDS]_0$.

126 For the reactant concentrations used in this study the plots in Figure S2 were obtained.

127

128   **Figure S2:** 1:1 (AQDS:H$_2$AQDS) binding dimer model. Prediction of the theoretical concentration profiles for AQDS, H$_2$AQDS,

129   and the QH as a function of SOC, calculated using the dimer model. The simulations are performed at fixed $[AQDS]_0$ of 10, 20,

130   30, and 40 mM and $K_{dim} = 80$ M^{-1}.

131

132   With increasing [AQDS]$_0$, it is evident that the proportion of dimer to the total concentration

133   grows in the presented cases, and the concentrations of individual molecular species exhibit

134   increasingly nonlinear variations with respect to the SOC. Consequently, it is essential to account

135   for the influence of dimer formation on fluorescence intensity, particularly at high concentrations,

136   in order to accurately quantify the SOC. The plate reader data in Figure 2(C) demonstrate that the

137   intensity of the 40 mM solution follows the same nonlinear trend as the H$_2$AQDS concentration.

138

139

140

141

142   **ESI 5: Theoretical background of concentration fields in flow devices**

143

144   In electrochemical flow devices, the temporal change of the concentration fields can be modeled

145   by the sum of mass-transport and electrochemical source terms, namely advection A_j, diffusion D_j,

146   electromigration ε_j and the (Butler-Volmer) source term S.

$$\frac{\partial C_j}{\partial t} = A_j + D_j + \varepsilon_j + S \tag{S5.1}$$

147   A_j describes the net flow through the electrode and is given by a function of the geometry u and

148   the gradient of the concentration of interest ∇C_j,

$$A_j = -u \cdot \nabla C_j \tag{S5.2}$$

149   D_j as derived by Fick's law can be calculated from the diffusion coefficient of the molecular

150   species d_j and the Laplacian of the concentration of interest $\nabla^2 C_j$,

$$D_j = d_j \cdot \nabla^2 C_j \tag{S5.3}$$

151   ε_j describes the bias of charged entities through the electric field and is given by the charge z_j,

152   Faraday's constant F, the gas constant R, the temperature T, and the electric field $-\nabla \phi_L$,

$$\varepsilon_j = \frac{z_j \cdot D_j \cdot F}{R \cdot T} \cdot \nabla \cdot (C_j \cdot \nabla \phi_L) \qquad \text{(S5.4)}$$

153 Adding all terms together we obtain the following partial differential Eq. A.1 for the temporal
154 change of the concentration as a function of current, potential and mass-transport:

$$\frac{\partial C_j}{\partial t} = -u \cdot \nabla C_j + d_j \cdot \nabla^2 C_j + \frac{z_j D_j F}{R \cdot T} \cdot \nabla \cdot (C_j \cdot \nabla \phi_L) + S_j \qquad \text{(S5.5)}$$

155 The connection between the applied potential and the current is given through the electrochemical
156 source term (Butler-Volmer equation) measuring the overall rate of the redox reaction of AQDS.
157 The source term can be computed given the overpotential (η), the geometric area of the electrode
158 interface (a), the reaction rate constant (k), the charge transfer coefficients of the respective redox-
159 state (α_i) as well as the concentration of the reactant in each redox-state (C_i).

$$S = a \cdot k \cdot C_A^{\alpha_A} \cdot C_B^{\alpha_B} \cdot \left[\exp\left(\frac{n_e \cdot F \cdot \alpha_A}{R \cdot T} \cdot \eta \right) - \exp\left(\frac{n_e \cdot F \cdot \alpha_B}{R \cdot T} \cdot \eta \right) \right] \qquad \text{(S5.6)}$$

160 The applied overpotentials cause the current response which is monitored over the duration of the
161 experiment. Consequently, current and overpotential as well as fluorescence intensity and
162 concentration can be directly related. Both pairs of physical parameters must be connected to
163 finally interpret the fluorescence data and derive conclusions about current, potential and flow.
164
165 **ESI 6: Data calibration and SOC mapping**
166 As part of our calibration procedure, we considered the fluorescence contributions of each
167 molecular species involved, i.e. AQDS, H_2AQDS and QH, which are required for proper
168 quantification of the local SOC. The various contributions are displayed schematically in Figure
169 S3.
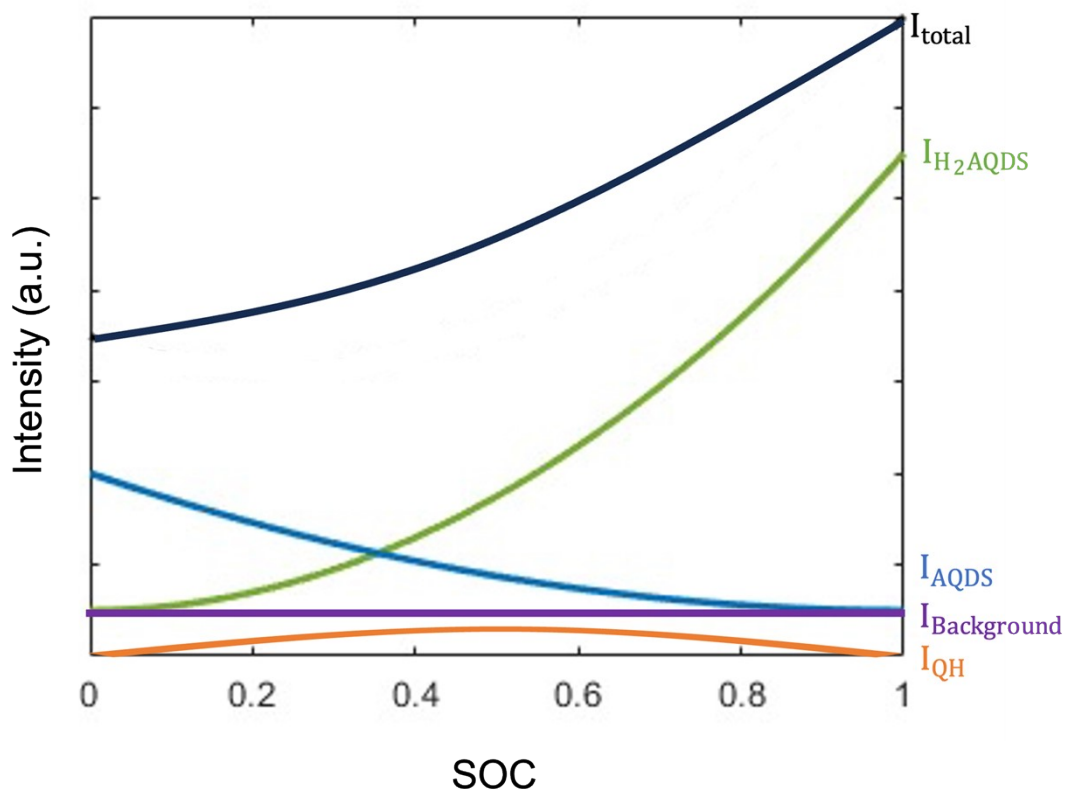
Figure S3: Schematic depiction (not to scale) of different contributions to the spatially averaged raw intensity I_{total}. For the calibration of the intensity maps to obtain SOC maps we need to distinguish between the different species contributing to I_{total}. The black solid line schematically shows I_{total} that is obtained in experiment. $I_{Background}$ is the background signal which remains constant in every image. I_{QH} corresponds to the dimer intensity which is expected to have small contribution to I_{tot} but is estimated independently. I_{AQDS} is the native fluorescence of AQDS and I_{H_2AQDS} is the fluorescence of H_2AQDS which has the highest contribution to I_{total}.

Our experimental data for the SOC estimation comprised 29 images. A single *ex situ* image taken at a high and homogeneous (but unknown) H_2AQDS concentration; and 28 images taken for varying applied overpotentials with 4 total AQDS concentrations crossed with 7 applied voltages. As the analysis is done at the individual pixel level, it is critical for the images to be aligned on that scale based on the *ex-situ* image. This was done using the CV2 computer vision library and resulted in a mean shift of 1.8 pixels. Once all the images were aligned, we assigned pixels into three categories: excessively dim; excessively bright; and reliable pixels to be included in the analysis. We hypothesize that excessively dim pixels were due to obstructing fibers, and excessively bright pixels were caused by highly reflective heterophase impurities. We set

187 thresholds for dim and bright pixels at quantiles 0.55 and 0.995, respectively. These thresholds

188 were set by a combination of a qualitative visual review of the data with a Gaussian mixture model

189 to set the lower threshold. As the location of the fibers remains fixed in every image, a pixel I_{ri} on

190 one of the reaction images was considered valid when the corresponding pixel B_i was valid on the

191 *ex-situ* image, and the pixel fell within the specified quantiles of intensity for that reaction. The

192 remaining pixels, corresponding to fibers and other heterophase impurities, were set to be NaN

193 and were not further considered in our analysis, as demonstrated for the example in Figure S4.

194

195
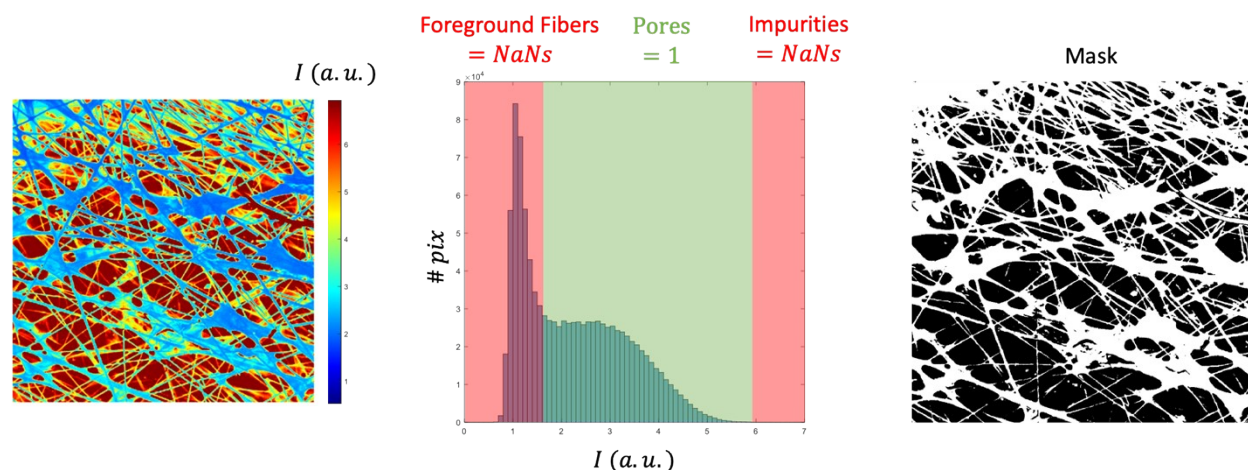
Figure S4: Selection of valid pixels for SOC maps. (Left) shows the raw intensity image in arbitrary units. (Middle) the histogram of the image is shown with schematic of the manually selected low and high intensity cutoffs. The red areas correspond to the pixels that were set to NaN values and are identified as fibers or impurities. The green area corresponds to the "good" pixels in the pores filled with electrolyte that are considered for further image processing. (Right) shows a visualization of the mask image that contains all valid pixels (in black) and NaN pixels in white.

201

202   This data filtering reduced the size of our calibration set from 29.4 million to 11.7 million

203 pixels. The result of the image data processing was an array of *ex situ* intensities B_i and arrays I_r

204 for each reaction condition.

205   We also had 28 utilizations u_r corresponding to each reaction and calculated by Eq. 3.2. We

206 posit a linear relationship between the electrochemical utilization u_r and the mean state of charge

207 $\bar{s}_r$. When the system is not mass transport limited, the mean field theory should be a highly accurate

208 approximation *on average* over a mesoscale patch of space, even if it does not hold uniformly over

209 very small areas. Most of our reactions had utilizations below 50%, justifying the claim that mass

210 transport limitations were not binding and the use of this approximation. In the simple mean field

211 theory without mass transport limitations, the solution is a smooth constant gradient in the state of

212 charge between 0 at the inlet and u at the outlet. The mean state of charge $\bar{S}$ and utilization u are

213 thus related by $\bar{S} = u x_m / L$ where x_m is the position of the midpoint of the image and L is the length

214 of the electrode. In our study, the ratio $x_m / L = 0.63$.

215   There are three electroactive species in this study, namely the oxidized state AQDS; the

216 reduced state H_2AQDS; and the dimer QH. The concentrations of these species are subject to two

217 constraints,

$$[AQDS] + [H_2AQDS] + 2\,[QH] = [AQDS]_0 \tag{S6.1a}$$

$$[QH] = K\,[AQDS]\,[H_2AQDS] \tag{S6.1b}$$

218 Eq. S6.1a is conservation of the anthraquninone species in their various forms, and Eq. S6.1b is

219 the chemical equilibrium governing dimer formation. It is straightforward to solve Eq. S6.1 for the

220 concentration of all three species using the relative concentration Y of the reduced species defined

221 in Eq. 3.5. The solutions are:

$$[AQDS] = \frac{1 - Y}{1 + 2\,R\,Y} \cdot [AQDS]_0 \tag{S6.2a}$$

$$[H_2AQDS] = Y \cdot [AQDS]_0 \tag{S6.2b}$$

$$[QH] = \frac{RY}{1 + 2\,R\,Y}\,[AQDS]_0 \tag{S6.2c}$$

222 where $R = K\,[AQDS]_0$ is the dimensionless rate constant for the dimer formation is.

223   We next made an initial estimate of the brightness coefficients α, β, γ, δ. To formulate this

224 estimate, we made the preliminary assumption (later relaxed in the final estimation) that the

225 concentrations of the electroactive species were uniform for each reaction. Using Eq. S6.2, we

226 constructed a numerical table mapping an input reduced fraction Y to an output state of charge.

227 There is one table for each initial concentration $[AQDS]_0$. These tables were all monotonically

228 increasing as we expected, and we used the data points to construct four numerical functions

229 mapping between SOC and Y at the various $[AQDS]_0$. We converted the utilizations u_r to a mean

230 SOC $\bar{S}_r$ for each reaction; interpolated $\bar{S}_r$ to obtain Y_r; and then solved for the equation of each

231 species using Eq. S6.2. We completed this step by solving a linear least squares problem of the

232 form $\mathbf{I} = \mathbf{XC}$. The left-hand side was the mean image intensity for the 28 reactions. The design

233 matrix $\mathbf{X}$ has 28 rows and four columns $[AQDS]$, $[H_2AQDS]$, $[QH]$, 1. The estimated coefficients

234 are $\mathbf{C} = [α, β, γ, δ]$. This regression achieved an excellent fit with an R squared value of 0.9632.

235 The estimated coefficients included a large, positive value for β (the brightness of H_2AQDS) and
236 much smaller values for AQDS and QH, as expected.

237   Once the brightness coefficients were available, we built a table with the predicted light
238 production P as a function of Y by Eq. 3.3. This led to a monotonic function that was interpolated
239 to produce a mapping function Y(P). We finally estimated the state of charge by applying Eq. 3.4
240 once we have the optical factor F_i at each pixel. We obtained the optical factor by applying the
241 assumption that the bright *ex situ* image is homogeneous, yielding the direct calculation $F_i = B_i/B$,
242 where B is the mean intensity on the ex-situ image. The resulting estimates of the state of charge
243 are visually plausible and have an excellent fit to the experimental brightness.

244   At this stage we made a further refinement of the model. We relinquished the assumption used
245 to estimate the brightness coefficients that the concentration was uniform on each reaction image.
246 We also insisted that the model recover the assumed mean state of charge on each reaction; the
247 initial estimate was close but had an RMS error of 0.031. This model was estimated by an iterative
248 application of three computational steps until convergence was achieved. These steps are: (1)
249 refine the estimate of the optical factor; (2) refine the estimate of the brightness coefficients; (3)
250 shift the estimated concentrations to match the mean state of charge S_r.

251   The concentration shifts are performed after applying a logit transform of the estimated Y for
252 each reaction. At each step, logit(Y) is shifted by one step of Newton's method using a numerical
253 derivative. Four steps of Newton's method are sufficient to match S_r to six decimal places. The
254 update to the brightness coefficients is analogous to the initial estimate. This time, however,
255 instead of a least squares problem with 28 rows (one per reaction), there are 11.7 million rows (one
256 per valid pixel). The left-hand side of the least squares equation is the observed intensity, and the
257 design matrix X is as before, but each row is now scaled by the optical factor. We can succinctly
258 write the design matrix entries as

259     $X_{ri} = [[AQDS], [H_2AQDS], [QH], 1] \cdot F_i$ This regression $\mathbf{I} = \mathbf{X}\,\mathbf{C}$ provides both an updated estimate
260 of the brightness coefficients and a standard error σ_I on the recovered brightness.

261   The update to the optical factors F is new to this stage of the estimation. If we consider pixel
262 *i* in isolation, Eq. 3.4 implies that we can construct a linear regression $\mathbf{I_r} = \mathbf{P_r}\,F$, where $\mathbf{I_r}$ and $\mathbf{P_r}$
263 are both column vectors with 28 rows, and F is the optical factor to be estimated. This regression

264 can be augmented to include an additional 29th row from the *ex situ* image with left and right sides
265 B_i and B, respectively. This regression also provides a standard error σ_F on the optical factor.

266   This model was initialized with preliminary estimates for the brightness coefficients and
267 optical factors described above. It was then iterated for nine steps until convergence criteria for
268 small changes in parameter values were met. The converged model includes estimates for the
269 concentration of all three species, from which we can easily compute the estimated SOC. The
270 model also estimates standard errors in I and F. We then compute a total standard error by
271 assuming that the errors in I and F are independent. The result of this calculation is an RMS error
272 of 0.00526 SOC units over all 28 reactions. The attribution of the error is 0.00422 due to
273 uncertainty in I and 0.00314 due to uncertainty in F. It is important to acknowledge that even after
274 the calibration procedure, certain residual background fibers and pore depth effects persisted,
275 which have the potential to introduce minor systematic errors.

276

277 *Comparison with a constant SOC gradient assumption:*
278 We assumed that over large scales, as the 1.2x1.2 mm imaging frame, a simplified assumption of
279 a constant SOC gradient along x and uniform along y can be used to estimate $\bar{S}$. The results are
280 then given by $\bar{S} = u x_m / L$ as demonstrated in Figure S5.

281

282
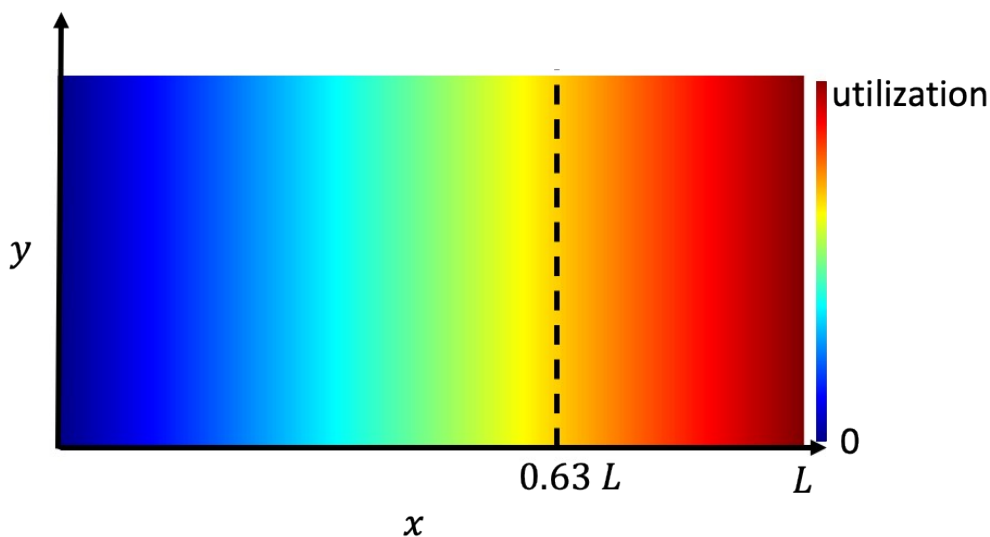
283

284   **Figure S5:** Schematic of simple constant gradient assumption. The rectangle corresponds to the working electrode where
285 the fully oxidized electrolyte enters on the left side and gets reduced in the form of a constant gradient along x towards the outlet.

286 The color map indicates the utilization of 0% in blue and the maximum utilization, at the end of the electrode, in red. In our

287 study, the image is centered at $x_m/L = 0.63$.

288

289 For a comparison of our results with the simple assumption of a smooth, constant gradient, we

290 generated simulated SOC maps at two distinct utilizations (0.3 and 0.6), maintaining x_m consistent

291 with the experimental location of the imaging center at 0.63L, as depicted in Figure S6. A mask

292 was superimposed on the images, designating pixels in regions obscured by fibers as NaNs.

293 Notably, the histograms indicate that the distributions largely resemble rectangular shapes, even

294 after the exclusion of the masked pixels.

295
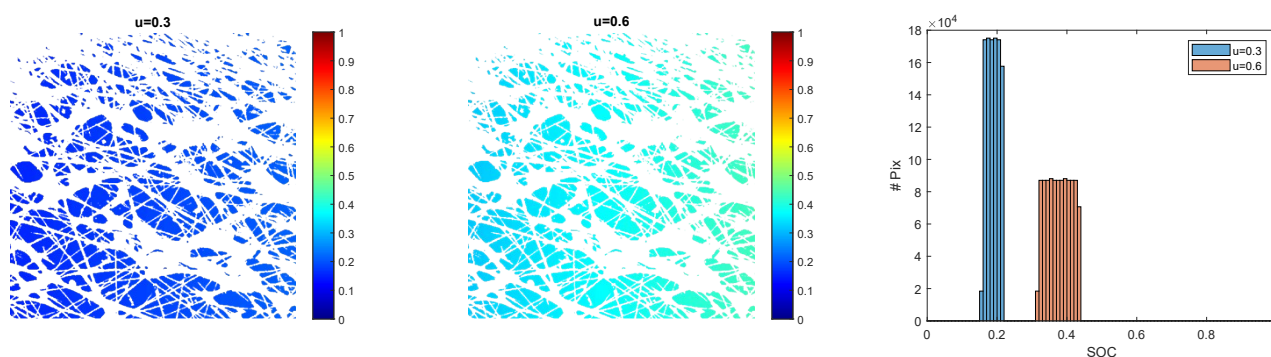
296
297 **Figure S6:** Spatial mapping of the simplified model featuring a constant gradient, tailored to the specific imaging frame and

298 incorporating the position and mask derived from the actual experiment. On the left, a simulated 2D SOC corresponds to an

299 electrolyte utilization of 0.3, while the central image represents a utilization of 0.6. The rightmost image presents the associated

300 histograms, which largely maintain rectangular distributions even in the presence of NaN values.

301 References

302 1.   Tong L, Chen Q, Wong AA, Gómez-Bombarelli R, Aspuru-Guzik A, Gordon RG, Aziz
303 MJ. UV-Vis spectrophotometry of quinone flow battery electrolyte for in situ monitoring and
304 improved electrochemical modeling of potential and quinhydrone formation. Physical Chemistry
305 Chemical Physics. 2017;19(47):31684-91.
306